Giant nonvolatile resistive switching in a Mott oxide and ferroelectric hybrid

Pavel Salev[a,1], Javier del Valle[a], Yoav Kalcheim[a], and Ivan K. Schuller[a]

[a]Department of Physics, Center for Advanced Nanoscience, University of California, San Diego, La Jolla, CA 92093

Edited by Laura H. Greene, Florida State University, Tallahassee, FL, and approved March 19, 2019 (received for review December 30, 2018)

Controlling the electronic properties of oxides that feature a metal–insulator transition (MIT) is a key requirement for developing a new class of electronics often referred to as "Mottronics." A simple, controllable method to switch the MIT properties in real time is needed for practical applications. Here we report a giant, nonvolatile resistive switching ($\Delta R/R > 1{,}000\%$) and strong modulation of the MIT temperature ($\Delta T_c > 30$ K) in a voltage-actuated V_2O_3/PMN-PT [$Pb(Mg,Nb)O_3$-$PbTiO_3$] heterostructure. This resistive switching is an order of magnitude larger than ever encountered in any other similar systems. The control of the V_2O_3 electronic properties is achieved using the transfer of switchable ferroelastic strain from the PMN-PT substrate into the epitaxially grown V_2O_3 film. Strain can reversibly promote/hinder the structural phase transition in the V_2O_3, thus advancing/suppressing the associated MIT. The giant resistive switching and strong T_c modulation could enable practical implementations of voltage-controlled Mott devices and provide a platform for exploring fundamental electronic properties of V_2O_3.

correlated oxide | metal–insulator transition | resistive switching | neuromorphic

Further advancement of computational technologies requires developing approaches beyond the traditional Turing–von Neumann architecture (1–3). One of the most promising alternatives is hardware-level neuromorphic computing, i.e., building a machine that mimics the operation of a brain (4–6). Such machine is proposed to be a large-scale network of simple computing units (neurons) performing a "leaky-integrate-and-fire" operation which are interlinked by nonvolatile memory elements (synapses). Because a human brain contains on the order of 10^{10} neurons and 10^{14} synapses, the implementation of a similar-complexity machine requires the development of simple circuits using ultralow power consumption artificial neurons and synapses (7). Transition metal oxides have the potential to become the material base for neuromorphic circuits. Oxides such as NbO_2, VO_2, V_2O_3, etc., that feature a metal–insulator transition (MIT), can be used to mimic the operation of neurons by taking advantage of the large ON/OFF-ratio threshold firing effect (8, 9). Continuous nonvolatile resistive modulation, necessary to implement an artificial synapse, can be achieved in a variety of oxides via multiple routes, for example, by utilizing electroforming (10), electrical gating (11, 12), by assembling ferroelectric tunnel junctions (13), etc. It would be desirable to develop a material system in which the threshold firing associated with the MIT and a controllable nonvolatile resistive switching are present simultaneously. This would enable assembling neuromorphic devices on a single-material platform, thus greatly simplifying the monolithic integration necessary for high-density circuits.

In this work we use the ferroelectric solid solution $Pb(Mg,Nb)O_3$-$PbTiO_3$ (PMN-PT) to apply electrically tunable stress on an epitaxial V_2O_3 film to modulate its electronic properties. V_2O_3 is a classic Mott insulator that has a first-order MIT accompanied by a rhombohedral-to-monoclinic structural transition at T_c = 150–160 K (14, 15). The phase transition in V_2O_3 thin films is highly sensitive to external forces such as hydrostatic pressure (16) and epitaxial strain (17–20). Oxide/ferroelectric hybrids had been studied before using other correlated materials, such as VO_2 (21–23), Fe_3O_4 (24), $LaNiO_3$ (25), and $NdNiO_3$ (26), having the largest reported resistive switching in the range of $1.5\% < \Delta R/R < 110\%$. In V_2O_3/PMN-PT, we achieved a nonvolatile resistive switching over 1,000% and a MIT temperature modulation over 30 K by switching the substrate between the single out-of-plane domain and multidomain polarization states. This discovery provides the means for engineering tunable memristive elements and can enable functionalities such as switching the device's operation between thermal (volatile) and electrochemical (nonvolatile) threshold-firing modes (27) by adjusting the material's T_c.

Results

Fig. 1*A* schematically shows the V_2O_3/PMN-PT device configuration and the electrical measurement circuit. The device is a parallel plate capacitor built from the V_2O_3 and Au electrodes that enclose the insulating PMN-PT. The circuit allows a four-probe measurement of the V_2O_3 resistance while simultaneously switching the PMN-PT's polarization via a bias voltage applied between the V_2O_3 and Au electrodes. Fig. 1*B* shows the polarization switching in a V_2O_3/PMN-PT/Au device at two temperatures. High-temperature treatment during the film growth (*Materials and Methods*) did not suppress the ferroelectricity in the PMN-PT. The measured hysteresis loops have well-defined saturation and switching regions. The PMN-PT's spontaneous polarization and coercive fields increase as the temperature decreases, as it is expected in a ferroelectric material. Even under high applied voltages, there were no measurable leakage currents that could cause Joule heating and affect the device's temperature.

Significance

New materials are currently investigated as a basis for energy-efficient computational paradigms such as neuromorphic computing. In materials exhibiting a metal–insulator transition (MIT), a small stimulus can trigger a large change in electrical conductivity. This can be used to mimic brain-spiking activity in biologically inspired electronics. Enabling continuous, nonvolatile, and reversible tuning of the MIT is important for implementing learning algorithms. Here we demonstrate an unprecedentedly large, voltage-controlled MIT temperature modulation and resistive switching in a Mott-oxide/ferroelectric heterostructure. Our results imply this effect is produced by strain tuning of the structural phase transition (SPT) which is coupled to the MIT. Since many Mott oxides have concurrent MIT and SPT, our results are directly relevant to a broad range of correlated oxides heterostructures.

Author contributions: P.S., J.d.V., and I.K.S. designed research; P.S., J.d.V., and Y.K. performed research; P.S., J.d.V., and Y.K. analyzed data; and P.S., J.d.V., Y.K., and I.K.S. wrote the paper.

The authors declare no conflict of interest.

This article is a PNAS Direct Submission.

[1]To whom correspondence should be addressed. Email: psalev@ucsd.edu.

This article contains supporting information online at www.pnas.org/lookup/suppl/doi:10.1073/pnas.1822138116/-/DCSupplemental.

Published online April 11, 2019.

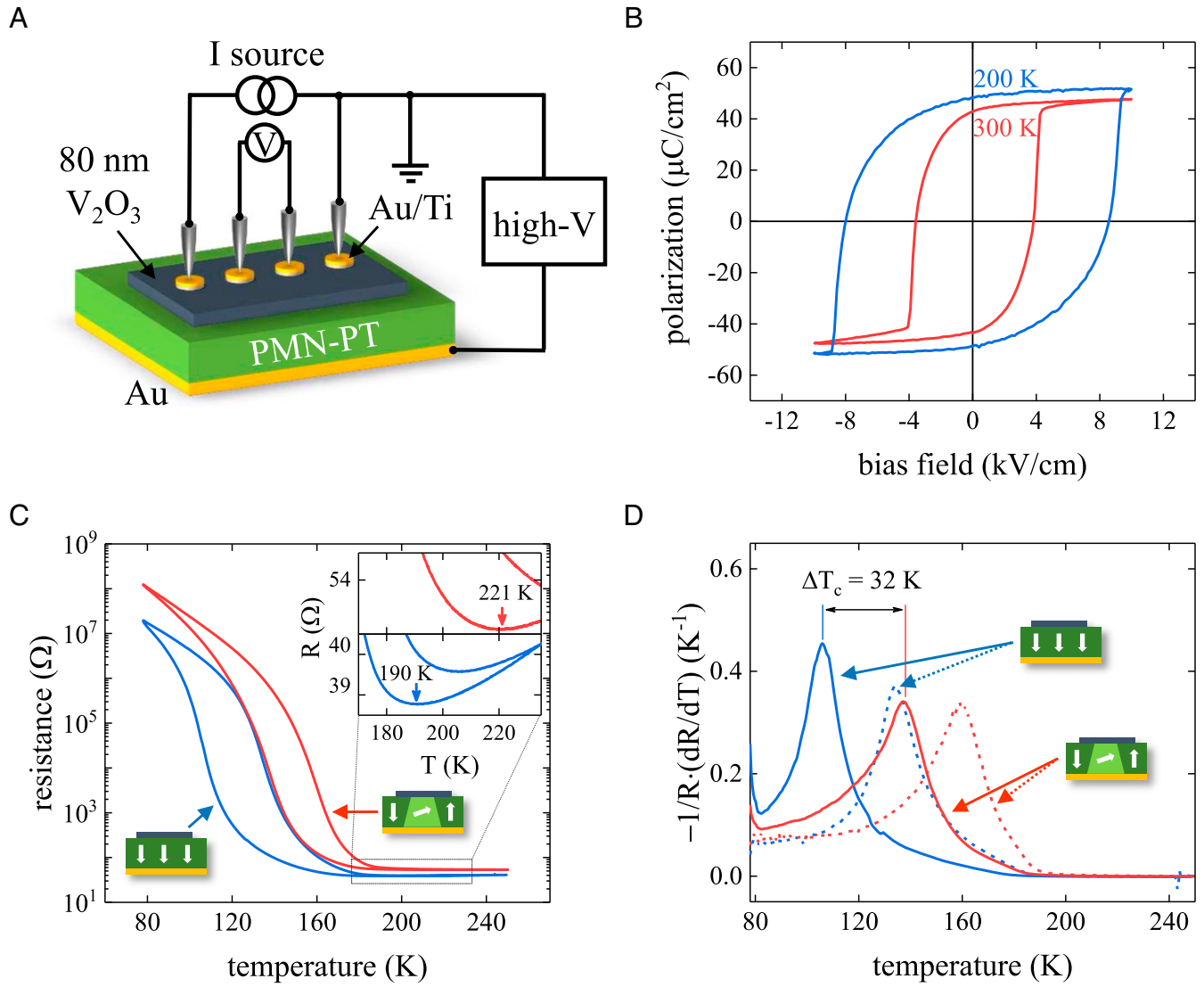

Fig. 1. Control of the MIT in V_2O_3/PMN-PT. (*A*) Schematic representation of the V_2O_3/PMN-PT device and the electric transport measurement circuit. (*B*) Polarization hysteresis loops of V_2O_3/PMN-PT/Au at 300 K (red line) and 200 K (blue line). (*C*) Nonvolatile control of the MIT in V_2O_3 film by switching the PMN-PT's polarization into the out-of-plane direction by a −10-kV/cm bias (blue line) and into a multidomain state by a +3.8-kV/cm bias (red line). Device pictograms schematically show the polarization domain configurations in the PMN-PT. (*Inset*) Magnification of the region where the R–Ts change the slope (marked with arrows), which indicates the beginning of insulating domains nucleation in the V_2O_3. (*D*) Resistance derivatives with respect to temperature. Continuous and dotted lines correspond to the cooling and heating cycles, respectively. The peaks indicate a rapid resistance change that can be attributed to the loss/establishment of electrical percolation in the V_2O_3.

The polarization domain configuration in the PMN-PT substrate has a major effect on the MIT of the V_2O_3 film. Fig. 1*C* shows two resistance vs. temperature (R–T) curves of a V_2O_3 device corresponding to the out-of-plane single domain (blue line) and multidomain (red line) polarization configurations in the PMN-PT. At the beginning of each measurement, the substrate was switched at 250 K. This was done by applying a −10-kV/cm bias (higher than the saturating field) to induce the single out-of-plane domain configuration and a +3.8-kV/cm bias (close to the coercive field) to switch the substrate into a multidomain configuration. Then an R–T was acquired under zero bias during a continuous temperature sweep. Both R–Ts in Fig. 1*C* show the characteristic MIT having over four orders of magnitude resistance change. Remarkably, changing the PMN-PT domain configuration shifts the V_2O_3 MIT by up to 32 K. This is further emphasized in the resistance derivatives plot (Fig. 1*D*) in which the peaks are associated with the loss/establishment of electrical percolation. The PMN-PT's domain configuration also affects the temperature of insulating domain nucleation in the V_2O_3, which causes the sign change of the R–T slope (Fig. 1*C*, *Inset*). The T_c modulation is nonvolatile and persists over a large temperature sweep range. The effect is fully reversible by switching the substrate between the out-of-plane and multidomain configurations. To the best of our knowledge, the ΔT_c = 32 K in V_2O_3/PMN-PT is at least 4–10× larger than in any other similar (correlated oxide)/(ferroelectric) heterostructures (21–24, 26, 28).

The same circuit as in Fig. 1*A* was used to investigate the nonvolatile resistive switching in the V_2O_3 controlled by a bias field on the PMN-PT. Fig. 2*A* shows the resistive switching ratio $\Delta R/R$ vs. bias field E recorded at three different temperatures. The resistive switching ratio is defined as $\Delta R/R(E) = 100\% [R(E) - R_0]/R_0$, where R_0 is the device's minimum resistance at zero bias. The $\Delta R/R$ loops have well-defined low- and high-resistance states and the switching between them occurs at a bias field close

to the PMN-PT coercive field. The magnitude of ΔR/R depends on the temperature. At T = 145 K, we observed the largest ΔR/R ~ 1,100%, which is one to two orders of magnitude higher than in any other similar (correlated oxide)/(ferroelectric) heterostructures (21–24). The temperature dependence of the zero-bias ΔR/R, i.e., the nonvolatile switching between the low- and high-resistance states, is shown in Fig. 2*B*. The largest ΔR/R coincides with the T_c of V_2O_3 indicating that the giant resistive switching is related to the MIT. Below the T_c, the ΔR/R remains within 50–100% range. Above the T_c, the ΔR/R slowly decreases from 40% at 180 K to 18% at room temperature.

The resistance of V_2O_3 devices can be tuned continuously between the low- and high-resistance states by adjusting the bias amplitude applied to the PMN-PT, as demonstrated in Fig. 2*C*. At the beginning of each measurement, the device was switched into the low-resistance state R_0 = 1.6 kΩ by applying −17-kV/cm bias to the PMN-PT. The application of +11-kV/cm bias switches the V_2O_3 into the high-resistance state of 18 kΩ, which corresponds to ΔR/R = 1,025%. If a bias field with an amplitude below +11 kV/cm is applied, then the V_2O_3/PMN-PT can be switched into an intermediate resistance state ranging between the low 1.6 kΩ and high 18 kΩ limits. This continuous, analog resistance tuning is the essential feature that is needed to implement an artificial synapse for hardware-level neuromorphic circuits.

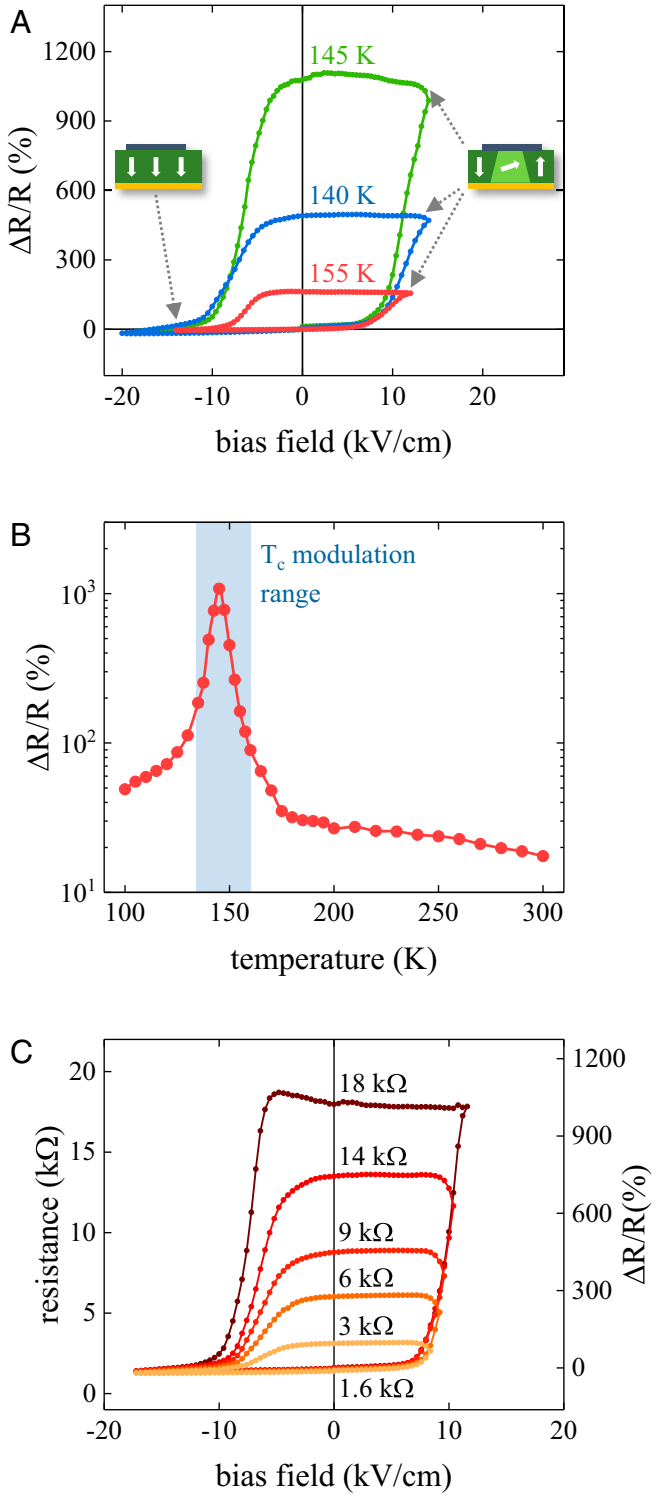

Fig. 2. Nonvolatile resistive switching in V_2O_3/PMN-PT. (*A*) Resistive switching ratio in the V_2O_3 film vs. the bias field applied to the PMN-PT substrate at three different temperatures. (*B*) Temperature dependence of the nonvolatile resistive switching ratio at zero bias. The shaded region corresponds to the T_c modulation range observed in the R–T measurements (Fig. 1*C*). (*C*) Analog resistive tuning in V_2O_3/PMN-PT achieved by adjusting the bias-field amplitude. The measurements were done at 145 K.

Discussion

We considered four possible mechanisms behind the nonvolatile control of the V_2O_3/PMN-PT electrical properties: (*i*) transfer of piezoelectric/ferroelastic strain from the substrate into the film that contracts/expands the V_2O_3 lattice, (*ii*) strain-mediated disorder induced in the V_2O_3 when the PMN-PT is switched into a polarization multidomain configuration, (*iii*) ion migration in the V_2O_3 caused by transient currents associated with the polarization switching in the PMN-PT, and (*iv*) field effect, i.e., accumulation/depletion of free carriers in the V_2O_3 to screen the spontaneous polarization of PMN-PT. Here we focus on the strain transfer effect, the primary driving force behind the resistive switching. A brief discussion on the strain-mediated disorder, ion migration, and field effect is available in *SI Appendix*.

The V_2O_3 resistance increases strongly only when the PMN-PT is switched into a multidomain configuration, being virtually unaffected by a 180° out-of-plane polarization reversal. A large-amplitude bias sweep, inducing a 180° polarization switching, results in a nearly symmetric "butterfly"-shaped resistive switching loop, in which the device always switches back into the low-resistance state at zero bias (Fig. 3*A*). The application of a bias close to the PMN-PT coercive field, inducing a multidomain state, switches the film into the high-resistance state independent of the initial "up" or "down" polarization direction in the substrate (Fig. 3 *B* and *C*).

To gain an insight into the structural difference between the low- and high-resistance states, we measured high-resolution reciprocal space maps (RSMs) in the vicinity of PMN-PT (111) Bragg peak (Fig. 3*D*). The rhombohedral PMN-PT lattice is elongated in the polarization direction that coincides with the space diagonals of the perovskite unit cell (29). There are eight equivalent polarization domain orientations in PMN-PT, all of which can emerge during the polarization switching. In a <111>-oriented substrate, two orientations correspond to the up and down out-of-plane polarization domains (OOP domains) and six orientations at 71°/109° with respect to the surface normal have a large in-plane polarization component (IP domains). We found that when the V_2O_3/PMN-PT is in the low-resistance state, the PMN-PT is nearly in a single OOP domain configuration. In the high-resistance state, ~40% of the substrate's volume comprises the IP domains. The IP domains are expected to induce a tensile in-plane strain in the V_2O_3 film; therefore, it is consistent with the V_2O_3 phase diagram (15) that the film's T_c increases when the PMN-PT is switched into a multidomain configuration. The measured difference of the spontaneous strains between the IP and OOP domains in the PMN-PT is ~0.27%. A similar lattice compression in a bulk V_2O_3 crystal can be induced by ~1-MPa hydrostatic pressure (30) which reduces

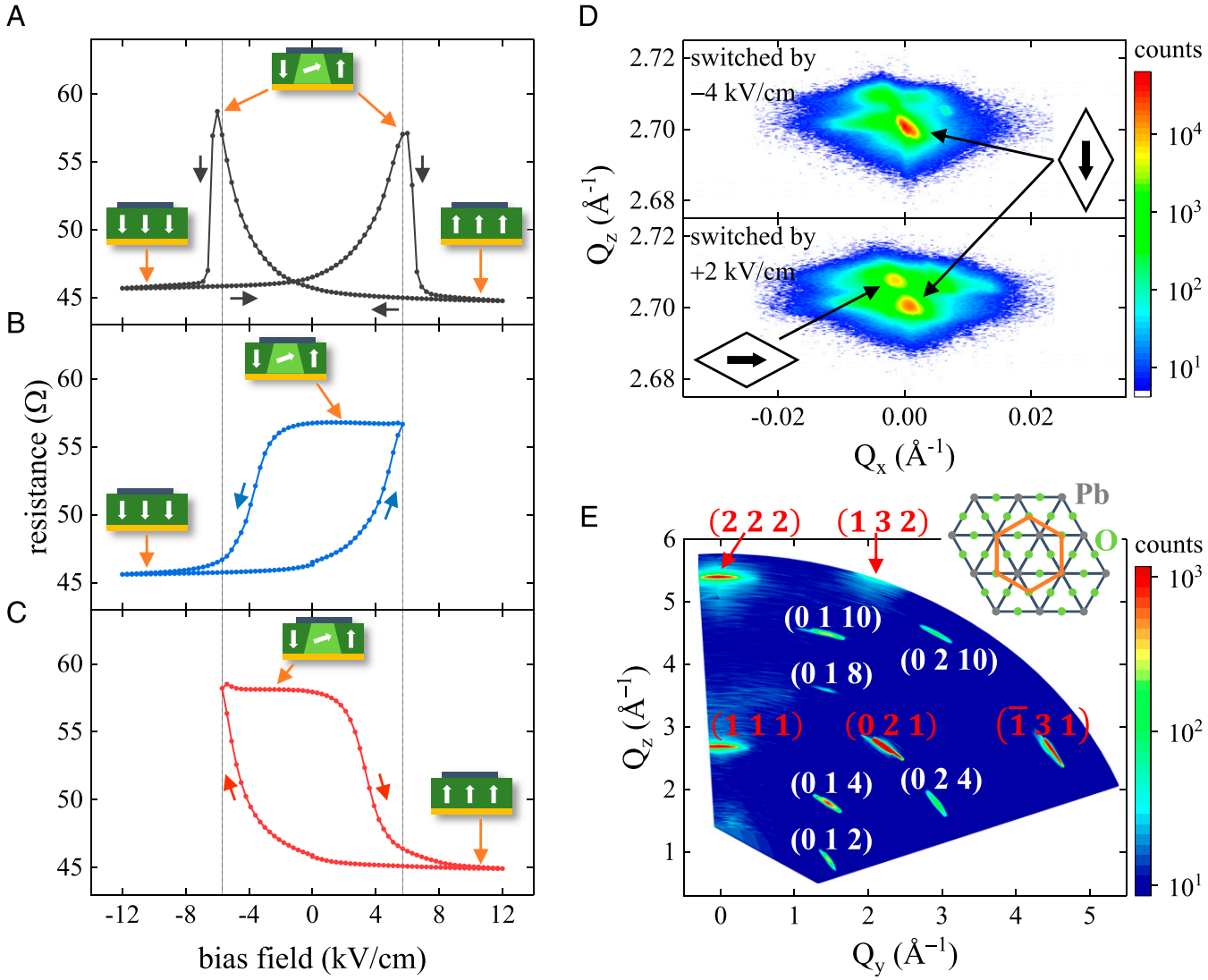

Fig. 3. Strain effect in V_2O_3/PMN-PT. (*A*–*C*) Resistive switching in V_2O_3/PMN-PT under a high- (*A*) and reduced-amplitude (*B* and *C*) bias fields. The high-amplitude bias (*A*) induces 180° out-of-plane polarization switching in the PMN-PT resulting in a symmetric butterfly-shaped resistive switching loop in the V_2O_3. The reduced-amplitude bias (*B* and *C*) switches the PMN-PT into a multidomain state producing a nonvolatile resistive switching in the V_2O_3. Measurements were done at 200 K to ensure that the full polarization saturation can be achieved in the experimental setup. (*D*) RSM in the vicinity of the PMN-PT (111) Bragg peak for the sample switched into the low- (*Top* plot) and high-resistance (*Bottom* plot) states. The Bragg peaks corresponding to the OOP and IP domains are marked in the plots. (*E*) Wide-range RSM of the V_2O_3/PMN-PT sample. The film and substrate peak indices are written in white and red, respectively. (*Inset*) The alignment of the corundum (001) plane of V_2O_3 (orange) with the (111) plane of PMN-PT (gray and green) is shown schematically.

its T_c by 40 K (15). This is close to the largest MIT temperature modulation $\Delta T_c = 32$ K observed in our samples, which indicates that the transfer of switchable strain from the substrate into the film gives rise to this effect. Additionally, the resistive switching in the V_2O_3/PMN-PT above the MIT can be described reasonably well by a simple hydrostatic-pressure–like model (*SI Appendix*), which further supports the strain transfer origin of this effect. Direct measurements of the switchable strain in the V_2O_3 thin film unfortunately proved unfeasible in our experimental setup. The film's Bragg peaks have too weak intensity for high-resolution measurements using a laboratory-based X-ray tool. Analysis of the strain in V_2O_3, however, could be possible using a high-brilliance X-ray source such as synchrotron radiation.

Efficient strain transfer from the PMN-PT into the V_2O_3 could be enabled by the epitaxial relation between the film and the substrate. In a V_2O_3 crystal, the *a* lattice parameter of the high-temperature corundum phase expands by +1.0% across the phase transition while the *c* parameter contracts slightly by –0.2% (14). In V_2O_3 films, the strain coupling of the film's (001) plane to a substrate has been found to strongly affect the MIT (31). In this work, we specifically chose (111)-oriented PMN-PT to promote the V_2O_3 film growth along its corundum *c* axis. The wide-range RSM measurements confirmed the epitaxial relation $(001)_{V2O3}||(111)_{PMN\text{-}PT}$ (Fig. 3*E*). Therefore, the switchable stress provided by the PMN-PT acts directly on the V_2O_3 (001) plane that is expected to have the largest size change across the structural phase transition; thus, the stress can suppress or promote the associated electronic MIT. The transfer of switchable strain was also identified as the origin of resistive switching in the related VO_2/PMN-PT system (21–23). The nonvolatile resistive switching in V_2O_3/PMN-PT, however, is at least 50× larger compared with the VO_2/PMN-PT. This may be due to a much greater sensitivity of V_2O_3 to a stress. For example, 2-GPa hydrostatic pressure shifts the T_c of VO_2 by ∼2 K (32, 33), while the same pressure completely suppresses the MIT in V_2O_3 (15).

V_2O_3/PMN-PT is a unique artificial system in which a sharp MIT and a large nonvolatile resistive switching are present at the

same time. This discovery could enable the development of a hardware-level, single-material, neuromorphic platform that is simultaneously capable of emulating the operations of neurons [using the MIT-based threshold firing (8, 9, 34)] and synapses (using the analog resistance tuning). The giant resistive switching $\Delta R/R > 1{,}000\%$ in V_2O_3/PMN-PT is related to the nucleation of polarization domains with an elongated in-plane lattice parameter in the substrate and the subsequent transfer of the ferroelastic strain into the film. The strain associated purely with the piezoelectric effect in the PMN-PT, on the other hand, has very little impact on the V_2O_3 resistance, $\Delta R/R < 10\%$ (*SI Appendix*). Therefore, the complex solid solution PMN-PT potentially can be substituted by "simpler" ferroelectrics, e.g., lead-free $BaTiO_3$ or $BiFeO_3$, in which a reversible switching between OOP and IP polarization configurations is possible. Further studies are needed to test whether the inherently inhomogeneous stress in a multidomain PMN-PT has a special impact on the V_2O_3 electronic properties and to investigate how the switchable stress reversibly drives the V_2O_3 film through the corundum-monoclinic structural phase transition. Addressing these questions may reveal the origin of the giant resistive switching in V_2O_3/PMN-PT and improve our knowledge of the complex physics of strongly correlated oxides, which may lead to transformative technological breakthroughs.

Materials and Methods

Film Growth and Device Fabrication. V_2O_3 films were grown epitaxially on <111>-oriented double-side–polished 0.5-mm-thick $0.7Pb(Mg_{1/3}Nb_{2/3})O_3$-$0.3PbTiO_3$ substrates by on-axis rf magnetron sputtering. V_2O_3 was sputtered in 7.8-mTorr pure Ar atmosphere from a stoichiometric ceramic target. The rf power supplied to the target was 150-W which resulted in ∼2.5-Å/s film growth rate. The film growth was done at a substrate temperature of 650 °C. After the growth, the samples were thermally quenched at ∼100 °C/min cooling rate (35). The synthesized films had the thickness of 80–100 nm as determined from X-ray reflectivity measurements (*SI Appendix*). Circular 150-μm-diameter (100 nm Au)/(20 nm Ti) electrodes for four-probe resistance measurements were fabricated on top of the V_2O_3 films using e-beam evaporation and a standard lift-off process. The $1{,}150 \times 550\text{-}\mu m^2$ rectangular V_2O_3 devices were patterned using reactive ion etching in a 50-mTorr 50/50 Cl_2/Ar atmosphere. A 120-nm-thick Au layer was evaporated on the back of PMN-PT to use as the bottom electrode for the polarization switching measurements.

Electrical Measurements. The measurements at cryogenic temperatures were performed in a Lakeshore TTPX probe station equipped with four electrical probes and a substrate holder biasing lead. The resistance of V_2O_3/PMN-PT devices was measured in a four-point configuration using a Keithley 6221 current source and a Keithley 2812 nanovoltmeter. The R–T curves (Fig. 1*C*) were acquired during a continuous temperature sweep at 1-K/min rate. The polarization switching in the PMN-PT substrate for the transport measurements was done using the voltage source of a Keithley 6517 electrometer (±1,000-V maximum output). The measurement circuit in Fig. 1*A* was designed to keep the V_2O_3 film close to the ground potential. This allowed accurate resistance measurements both with and without a bias field applied to the substrate. The polarization hysteresis loops (Fig. 1*B*) in the V_2O_3/PMN-PT/Au devices were recorded using a Radiant Premier II tester.

Structural Characterization. The XRD measurements were done in Rigaku SmartLab system at room temperature. Unpatterned V_2O_3/PMN/PT samples were used in the X-ray measurements. The RSMs in the vicinity of PMN-PT (111) Bragg peak for the sample switched into the low- and high-resistance states (Fig. 3*D*) were recorded by applying a bias field to the sample in situ before the measurements via electrical leads attached to the V_2O_3 top and Au bottom layers. The in situ bias setup ensured that the sample alignment does not change between each measurement. The wide-range RSM (Fig. 3*E*) was reconstructed from a series of θ-2θ scans recorded at different sample tilt angles in the plane orthogonal to the scattering plane (χ-angle). A set of standard measurements (reflectivity, rocking curves, pole figures) is available in *SI Appendix*, Fig. S1.

ACKNOWLEDGMENTS. We acknowledge support from the Vannevar Bush Faculty Fellowship program sponsored by the Basic Research Office of the Assistant Secretary of Defense for Research and Engineering and funded by the Office of Naval Research through Grant N00014-15-1-2848. J.d.V. thanks Fundación Ramón Areces for the funding.

1. Ladd TD, et al. (2010) Quantum computers. *Nature* 464:45–53.
2. Di Ventra M, Traversa FL (2018) Perspective: Memcomputing: Leveraging memory and physics to compute efficiently. *J Appl Phys* 123:180901.
3. Furber S (2016) Large-scale neuromorphic computing systems. *J Neural Eng* 13: 051001.
4. Schuller IK, Stevens R, Pino R, Pechan M (2015) *Neuromorphic Computing–From Materials Research to Systems Architecture Roundtable* (US Department of Energy). Available at https://science.energy.gov. Accessed March 29, 2019.
5. Ambrogio S, et al. (2018) Equivalent-accuracy accelerated neural-network training using analogue memory. *Nature* 558:60–67.
6. Ziegler M, Wenger C, Chicca E, Kohlstedt H (2018) Tutorial: Concepts for closely mimicking biological learning with memristive devices: Principles to emulate cellular forms of learning. *J Appl Phys* 124:152003.
7. Snider GS (2008) Spike-timing-dependent learning in memristive nanodevices. *2008 IEEE International Symposium on Nanoscale Architectures* (IEEE, Piscataway, NJ), pp 85–92.
8. Pickett MD, Medeiros-Ribeiro G, Williams RS (2013) A scalable neuristor built with Mott memristors. *Nat Mater* 12:114–117.
9. Ignatov M, Ziegler M, Hansen M, Petraru A, Kohlstedt H (2015) A memristive spiking neuron with firing rate coding. *Front Neurosci* 9:376.
10. Wong HSP, et al. (2012) Metal-oxide RRAM. *Proc IEEE* 100:1951–1970.
11. Ji H, Wei J, Natelson D (2012) Modulation of the electrical properties of VO_2 nanobeams using an ionic liquid as a gating medium. *Nano Lett* 12:2988–2992.
12. Shi J, Ha SD, Zhou Y, Schoofs F, Ramanathan S (2013) A correlated nickelate synaptic transistor. *Nat Commun* 4:2676.
13. Garcia V, Bibes M (2014) Ferroelectric tunnel junctions for information storage and processing. *Nat Commun* 5:4289.
14. McWhan DB, Remeika JP (1970) Metal-insulator transition in $(V_{1-x}Cr_x)_2O_3$. *Phys Rev B* 2:3734–3750.
15. McWhan DB, Menth A, Remeika JP, Brinkman WF, Rice TM (1973) Metal-insulator transitions in pure and doped V_2O_3. *Phys Rev B* 7:1920–1931.
16. Valmianski I, Ramirez JG, Urban C, Batlle X, Schuller IK (2017) Deviation from bulk in the pressure-temperature phase diagram of V_2O_3 thin films. *Phys Rev B* 95:155132.
17. Schuler H, Klimm S, Weissmann G, Renner C, Horn S (1997) Influence of strain on the electronic properties of epitaxial V_2O_3 thin films. *Thin Solid Films* 299:119–124.
18. Yonezawa S, Muraoka Y, Ueda Y, Hiroi Z (2004) Epitaxial strain effects on the metal-insulator transition in V_2O_3 thin films. *Solid State Commun* 129:245–248.
19. Dillemans L, et al. (2012) Correlation between strain and the metal-insulator transition in epitaxial V_2O_3 thin films grown by Molecular Beam Epitaxy. *Thin Solid Films* 520:4730–4733.
20. Thorsteinsson EB, Shayestehaminzadeh S, Arnalds UB (2018) Tuning metal-insulator transitions in epitaxial V_2O_3 thin films. *Appl Phys Lett* 112:161902.
21. Nan T, Liu M, Ren W, Ye ZG, Sun NX (2014) Voltage control of metal-insulator transition and non-volatile ferroelastic switching of resistance in VO_x/PMN-PT heterostructures. *Sci Rep* 4:5931.
22. Zhi B, et al. (2014) Electric-field-modulated nonvolatile resistance switching in VO_2/PMN-PT(111) heterostructures. *ACS Appl Mater Interfaces* 6:4603–4608.
23. Hong B, et al. (2017) Dynamic strain control of the metal–insulator transition and non-volatile resistance switching in (010) VO_2/(111) $Pb(Mg_{1/3}Nb_{2/3})_{0.7}Ti_{0.3}O_3$ epitaxial heterostructures. *Mater Lett* 196:108–111.
24. Liu M, et al. (2013) Non-volatile ferroelastic switching of the Verwey transition and resistivity of epitaxial Fe_3O_4/PMN-PT (011). *Sci Rep* 3:1876.
25. Marshall MSJ, et al. (2014) Conduction at a ferroelectric interface. *Phys Rev Appl* 2: 051001.
26. Heo S, et al. (2016) Modulation of metal-insulator transitions by field-controlled strain in $NdNiO_3$/$SrTiO_3$/PMN-PT (001) heterostructures. *Sci Rep* 6:22228.
27. Del Valle J, et al. (2017) Electrically induced multiple metal-insulator transitions in oxide nanodevices. *Phys Rev Appl* 8:054041.
28. Petraru A, Soni R, Kohlstedt H (2014) Voltage controlled biaxial strain in VO_2 films grown on $0.72Pb(Mg_{1/3}Nb_{2/3})$-$0.28PbTiO_3$ crystals and its effect on the transition temperature. *Appl Phys Lett* 105:092902.
29. Park SE, Shrout TR (1997) Ultrahigh strain and piezoelectric behavior in relaxor based ferroelectric single crystals. *J Appl Phys* 82:1804–1811.
30. Sato Y, Akimoto SI (1979) Hydrostatic compression of four corundum-type compounds: α-Al_2O_3, V_2O_3, Cr_2O_3, and α-Fe_2O_3. *J Appl Phys* 50:5285.
31. Brockman J, Samant MG, Roche KP, Parkin SSP (2012) Substrate-induced disorder in V_2O_3 thin films grown on annealed c-plane sapphire substrates. *Appl Phys Lett* 101: 051606.
32. Berglund CN, Jayaraman A (1969) Hydrostatic-pressure dependence of the electronic properties of VO_2 near the semiconductor-metal transition temperature. *Phys Rev* 185:1034–1039.
33. Chen Y, et al. (2017) Pressure-temperature phase diagram of vanadium dioxide. *Nano Lett* 17:2512–2516.
34. Stoliar P, et al. (2017) A leaky-integrate-and-fire neuron analog realized with a Mott insulator. *Adv Funct Mater* 27:1604740.
35. Trastoy J, Kalcheim Y, del Valle J, Valmianski I, Schuller IK (2018) Enhanced metal–insulator transition in V_2O_3 by thermal quenching after growth. *J Mater Sci* 53:9131–9137.